Median-Based Robust Algorithms for Tracing Neurons From Noisy Confocal Microscope Images

Khalid A. Al-Kofahi, Ali Can, *Member, IEEE*, Sharie Lasek, Donald H. Szarowski, Natalie Dowell-Mesfin, William Shain, James N. Turner, and Badrinath Roysam, *Member, IEEE*

Abstract—This paper presents a method to exploit rank statistics to improve fully automatic tracing of neurons from noisy digital confocal microscope images. Previously proposed exploratory tracing (vectorization) algorithms work by recursively following the neuronal topology, guided by responses of multiple directional correlation kernels. These algorithms were found to fail when the data was of lower quality (noisier, less contrast, weak signal, or more discontinuous structures). This type of data is commonly encountered in the study of neuronal growth on microfabricated surfaces. We show that by partitioning the correlation kernels in the tracing algorithm into multiple subkernels, and using the median of their responses as the guiding criterion improves the tracing precision from 41% to 89% for low-quality data, with a 5% improvement in recall. Improved handling was observed for artifacts such as discontinuities and/or hollowness of structures. The new algorithms require slightly higher amounts of computation, but are still acceptably fast, typically consuming less than 2 seconds on a personal computer (Pentium III, 500 MHz, 128 MB). They produce labeling for all somas present in the field, and a graph-theoretic representation of all dendritic/axonal structures that can be edited. Topological and size measurements such as area, length, and tortuosity are derived readily. The efficiency, accuracy, and fully-automated nature of the proposed method makes it attractive for large-scale applications such as high-throughput assays in the pharmaceutical industry, and study of neuron growth on nano/micro-fabricated structures. A careful quantitative validation of the proposed algorithms is provided against manually derived tracing, using a performance measure that combines the precision and recall metrics.

Index Terms—Biomedical image processing, image analysis, image edge analysis, image line pattern analysis, image processing, image segmentation, median filters.

I. INTRODUCTION

THE quantitative morphology of linear branched structures such as blood vessels and neurons is of broad interest [1]–[9]. Currently, much of the tracing is still conducted semiautomatically. A human user interacts with a microscope that is enhanced with computer imaging hardware and software (e.g., Neurolucida). The user performs pattern recognition and the computer system records the data, and generates morphometric summaries. In some cases, the computer assists the human by automatically aligning a cursor to the nearest image feature, or by automatically focusing the microscope [1], [10]–[12].

This paper presents a new generation of automated tracing algorithms that perform morphometry of neurons, especially those grown on man-made surfaces. This type of work has a variety of applications, including the documentation of neuronal development, neuronal responses to trauma and disease, and neurotoxicology assays. Fig. 1 presents a sample image of neurons grown on a patterned silicon substrate and labeled immunocytochemically, along with automatically generated traces of the dendrites and axons. Underlying these traces is a graph-theoretic representation that captures the neurons essential morphological characteristics. A number of topological and metric analyses could be conducted with such a representation [1].

In earlier work, this group has described fast and effective model-based algorithms for automatic tracing of linear branched structures, such as neurons, in three-dimensional volumetric images [13], and vasculature [8]. These methods are based on the modeling assumption that the structures of interest are bounded by nearly parallel edges. The present work was motivated by the failure of these otherwise robust and efficient algorithms, when the images of interest are very noisy. Fig. 2 shows such an example. Such high-noise images are unavoidable. *Increasing the laser power on the instrument to achieve a higher signal level leads to increased photodamage resulting in poor image quality and the possibility that fine structures may not be imaged*. Minimizing photodamage also precludes the use of slow scan image recording or signal integration at the time of image recording. These methods substantially improve the signal-to-noise ratio but they also significantly increase the total irradiation. Even if noise is minimized, the issue of apparent structural discontinuity remains. In other words, neuronal processes can appear discontinuous due to noninstrumentation reasons such as nonuniform dye absorption. The main contribution of the present paper is a method to
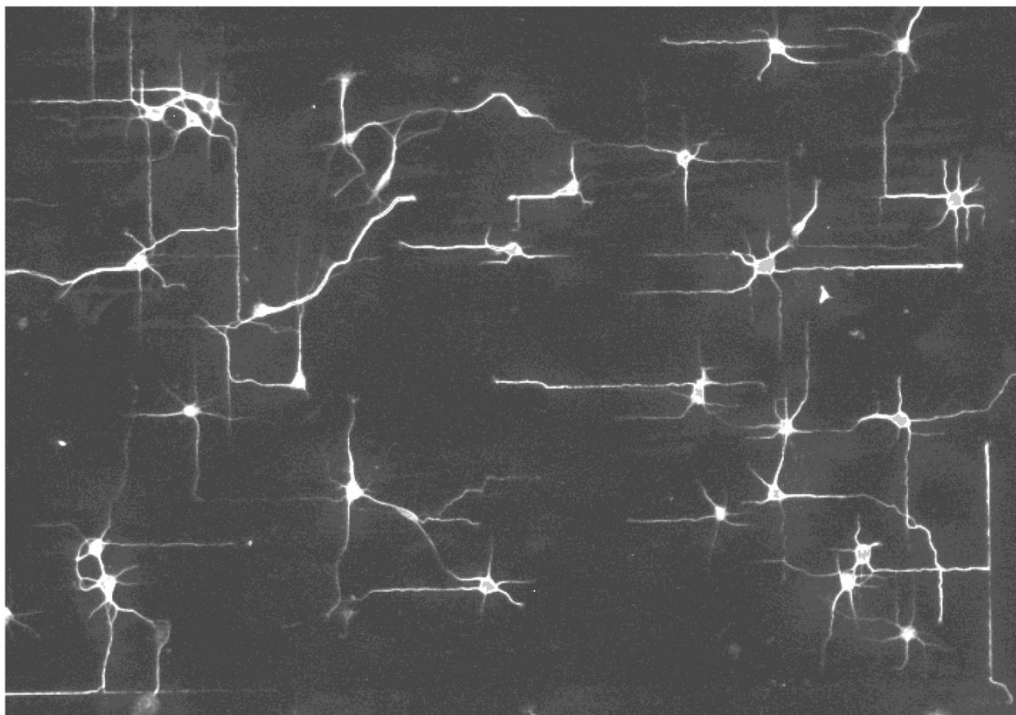
(a)
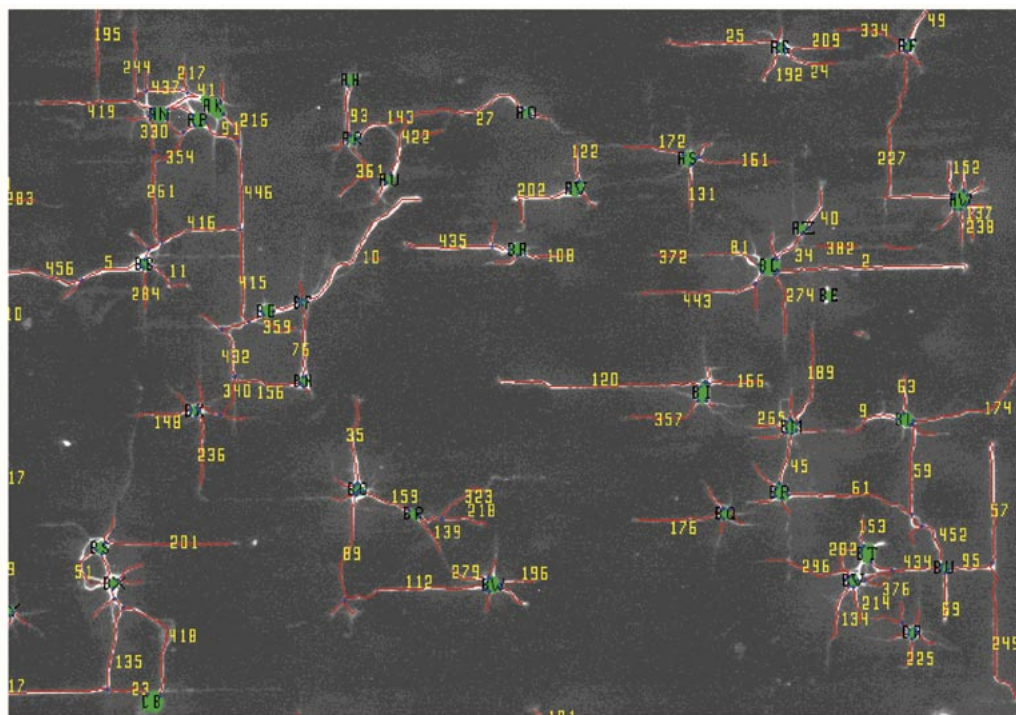
(b)

Fig. 1. (a) Laser-scanning confocal microscope image of multiple neurons growing on a patterned silicon substrate width 1175 μm, (b) the corresponding automatically generated and labeled traces. In this low-noise example, a traditional correlation-based tracing algorithm generates excellent results.

address the compelling need to perform fully automatic tracing when the structures of interest appear to be discontinuous due to noise and nonuniform contrast. The main idea is the use of median statistics instead of correlation operators used in prior work.

II. IMAGE ANALYSIS BACKGROUND

Three approaches are recognized for analysis of linear branched structures such as neurons and vasculature. The first is based on skeletonization and branch point analysis [e.g., [14]–[18]]. The second is based on enhancing edge/line proper-

(a)
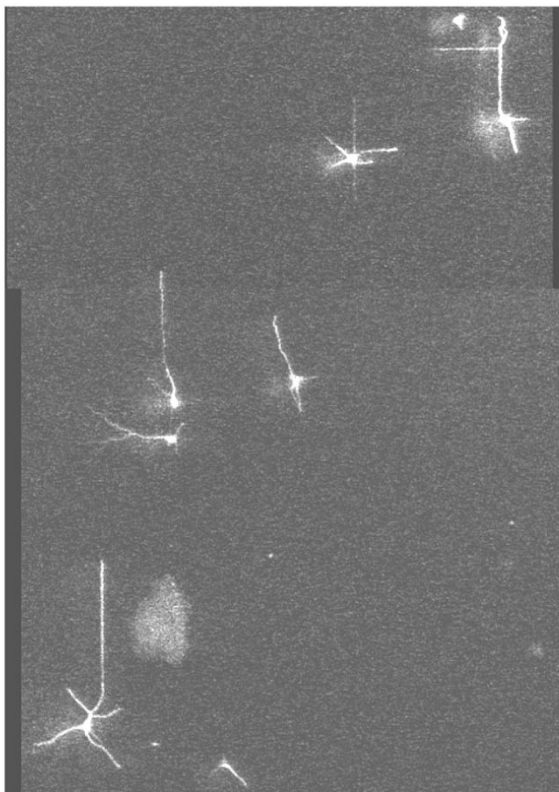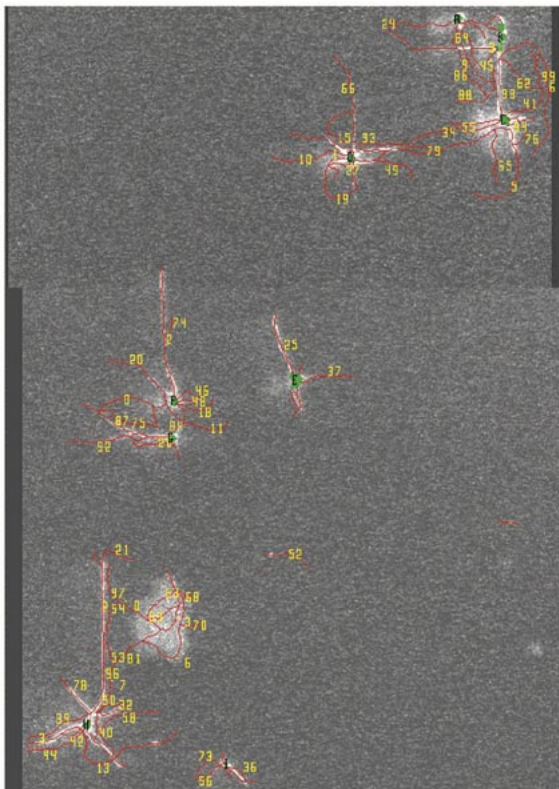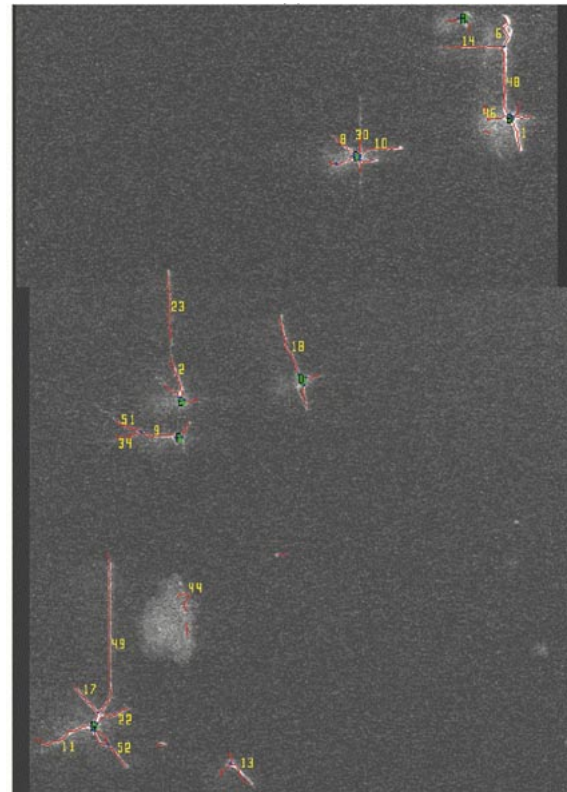
(c)

Fig. 2. *(Continued.)* Illustrating poor tracing performance in the presence of high imaging noise. (c) The automatically generated and labeled traces using the median based algorithm, all other settings being the same.

(b)

Fig. 2. Illustrating poor tracing performance in the presence of high imaging noise. (a) A low SNR laser-scanning confocal microscope image of multiple neurons growing on a patterned silicon substrate. (b) The automatically generated and labeled traces using the average based algorithm. (c) The automatically generated and labeled traces using the median based algorithm, all other settings being the same.

ties and then identifying process or vessel contours by chaining edge pixels together [19]–[26]. Both approaches require the processing of every image pixel with numerous operations per pixel; hence, they tend to scale poorly with image size. The third approach, exemplified by this paper and others, is referred to variously as vectorization, vectorial tracking, or exploratory tracing [7], [8], [27]. These methods work by first locating an initial point, and then exploiting local image properties to trace the structures recursively [8], [28].

Broadly, three categories of exploratory processing techniques are described in the literature. In the first category, the initial and end points of a vessel are entered manually (sometimes a tentative centerline is also provided) [19]–[21], [29]–[35]. In the second category, the algorithm starts with a manually entered initial point and an initial direction, and recursively tracks the entire arterial tree [7], [36], [37] using a breadth-first search. In the context of neuron images, this would correspond to tracing a single axon/dendrite tree that is efferent from a single neuron. Clearly, such methods are not suitable for images containing several neurons with each neuron having several processes efferent from it, and when neurons are large enough that only partial views are feasible. The third category, including this work, consists of fully automated methods [8] that overcome the limitations of the first two.

The core algorithm presented here builds upon the prior work of Sun [27], and our prior work [8], [13]. In particular, we employ an adaptive two-dimensional (2-D) kernel as opposed to

the fixed 2-D kernel used by Can *et al.* [8] and the one-dimensional (1-D) kernel used by Sun [7]. The adaptive kernel method enables the algorithm to trace over apparent discontinuities in the dendritic/axonal structures. Further robustness is achieved by simultaneously detecting both edges of the dendrite/axon structures.

Canny's edge detection algorithm [38], considered to be the standard for edge detection, involves smoothing, directional filtering, gradient computation, nonmaximum suppression, thresholding and edge-linking applied to all the pixels [39], [40]. Canny analyzed the tradeoff between edge detection and localization, and derived optimal filters for detecting edges. He showed that a Gaussian-smoothing prior to gradient computation is a good approximation to an optimal filter for step edges. The use of a Gaussian filter simplifies the implementation, because it is separable. Canny also showed that both localization and detection could be improved simultaneously by increasing the length of the filter along the edge direction as much as posible. However, the length of the directional filter should be chosen carefully. Canny's directional operator is formed by smoothing using a Gaussian kernel, differentiating normal to the edge direction, and then sampling along the hypothesized direction. For a given pixel, the response of the filters must be computed for different support, scale and orientation values. In our work, the scale is fixed, and the support and orientation are adaptively adjusted to significantly reduce the search space. The major innovation here is the use of a median based filter along the edge direction. The detection function used here is a low-pass differentiator (LPD) of the form $[-1, -2, 0, 2, 1]^T$, and the projection is a moving average with a support size of K pixels (Fig. 3). The length of the kernel, K, is set adaptively to establish better localization and detection as well as dynamically linking broken edges. Correlating a template with an image computes all of the above operations at once rather than applying them in a sequential manner such as in Canny [38]. This contributes to the robustness and effectiveness of our tracing algorithms. The algorithms compute the templates on a locally relevant portion of the image, which makes them computationally appealing as well. The template response at a location **p** along the orientation **u** is expressed as:

$$R(\mathbf{p}, \mathbf{u}) = \frac{1}{K} \sum_{j=1}^{K} r(\mathbf{p} + j\mathbf{u}, \mathbf{u}_\perp), \quad (1)$$

where $r(\mathbf{p}, \mathbf{u}_\perp)$ is the response of the 1-D LPD kernel at **p** along the direction $\mathbf{u}_\perp$ which is perpendicular to **u**, and K is the length of the template (see Fig. 3). Boundary points are estimated as those resulting in maximum template responses. Since the directional templates are separable, the filter response computed in (1) can be interpreted as averaging the LPD responses along the edge direction. Therefore, we will refer to the response of this set of directional templates as "Average Response". In Section IV, we describe a new set of templates where the averaging along the edge direction is replaced by median filtering. We will refer the response of this new set of templates as "Median Response".
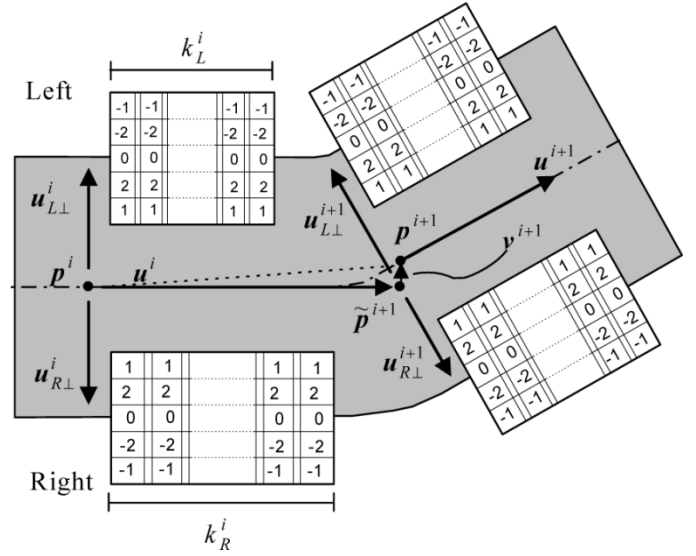

Fig. 3. Illustrating the exploratory tracing algorithm. Starting from centerline point $\boldsymbol{p}^i$, and initial direction $\boldsymbol{u}^i$ the perpendicular directions $\boldsymbol{u}_{L\perp}^i$ and $\boldsymbol{u}_{R\perp}^i$ are searched for the left and right boundaries, where the correlation responses are maximal. A step is taken along the direction of maximal response to $\tilde{\mathbf{p}}^{i+1}$. This is corrected by vector $\boldsymbol{v}^{i+1}$ to the next centerline point $\boldsymbol{p}^{i+1}$. The next tracing direction $\boldsymbol{u}^{i+1}$ is a weighted average combining $\boldsymbol{u}^i$ and the directions of the maximal-response kernels at step $i + 1$. The kernel lengths k_R^i and k_L^i are set adaptively, and can be different.

III. METHODS

Soma and dendritic structures are assumed to have higher intensity values than the surrounding background, and the dendrites/axons have roughly parallel and continuous boundaries. Fig. 1 shows a sample image along with the resulting traces. In addition to the image, the program generates a text output showing the size and the location of the somas, and length, width and location of the neurons. In this section we present those aspects of the tracing algorithms necessary to illustrate the differences between the two kernel types. We do not discuss other parts of the system described elsewhere [13], such as the soma detection and the seed point selection algorithms, both of which are necessary for the system's operation.

A. Exploratory Tracing

The $5 \times K$ kernel given in (1) and shown in Fig. 3 is referred to as a "template." Separate templates are constructed for the left and right boundaries of the structures, along different orientations. The orientations are discretized to a small number of values, typically 16 or 32. As illustrated in Fig. 3, starting from centerline point (mid-point between the process or vessel boundaries) $\mathbf{p^i}$, and the orientation, $\mathbf{u}^i$, of the process at this location, the next centerline point along the process is estimated by an update equation of the form

$$\mathbf{p^{i+1}} = \mathbf{p^i} + \alpha \mathbf{u^i}, \quad (2)$$

where α is a step size. The above update equation produces nonsmooth traces, especially when the local curvature is high. As illustrated in Fig. 3, smoother traces are obtained by adding a fine-tuning step to (2), resulting in the following update equations:

$$\tilde{\mathbf{p}}^{i+1} = \mathbf{p^i} + \alpha \mathbf{u^i}; \quad (3\text{-a})$$

$$\mathbf{p}^{i+1} = \tilde{\mathbf{p}}^{i+1} + \mathbf{v}^{i+1}, \quad (3\text{-b})$$
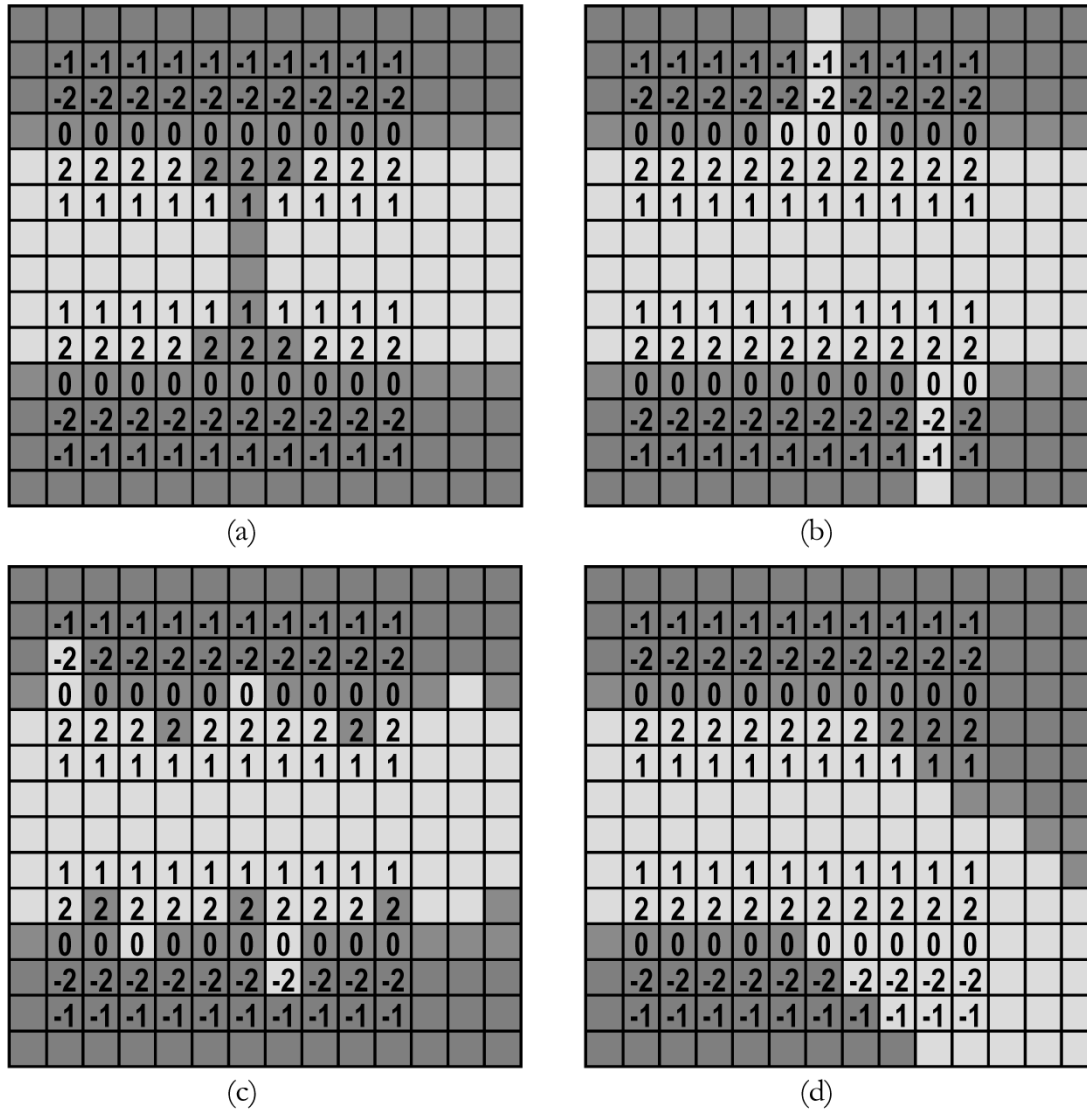
Fig. 4. Illustrating the response of the median based template for different types of artifacts for a horizontal segment. If the background intensity value is one and the foreground intensity value is 2, then the total median response is 6 for all the cases, whereas the total average response is 4.6, 5.4, 4.6, and 3.9 for Figs. *a*, *b*, *c*, and *d* respectively. Panel (a) illustrates a discontinuity. As long as the break is less than half the size of the template, the boundaries are linked successfully. Panel (b) shows protrusion artifacts. These structures cause the mean template based tracing to stop prematurely, but the median based template is robust to such artifacts as long as the width of such distortions is less than half of the template size. Panel (c) is a case of severely corrupted boundaries. As long as half or more of the pixels are not distorted, the median based template gives the desired response. Panel (d) illustrates the robustness of the median template when the length of the template is overestimated at regions of high curvature.

where $\mathbf{v}^{i+1}$ is a correction (fine-tuning) vector, and "$\sim$" indicates approximation. The correction vector is calculated by averaging the left and right boundary locations where the template response on each boundary is locally a maximum. The template response is computed using (1). The orientation space is discretized to N values, where N is set by the user to best sample the curvature of the structures of interest. For the results presented here, we used $N = 32$ yielding an angular precision of $11.25°$ and a total of 64 *left* and *right* templates. For a detailed description of the tracing algorithm, see [8], [13].

As illustrated in the next section, the tracing algorithm described above has demonstrated excellent performance when applied to images with good contrast and high SNR. However, it failed to trace images with low contrast and/or low SNR ratio.

Even when it was able to trace such low contrast images, it generated too many false positives (background) traces. Accurately and robustly tracing such image features is the motivation behind the present work.

IV. ROBUST TEMPLATES AND TRACING ALGORITHMS

Estimators based on order statistics are used preferentially in computer vision applications where the data are distorted by outliers [47]. Mean estimators are known to have a breakdown point of 0% [46], as opposed to median estimators that have a breakdown point of 50%. In image processing median-based statistics appear as median filters, known to be robust to impulsive or pepper-and-salt noise [45]. These types of noise can be
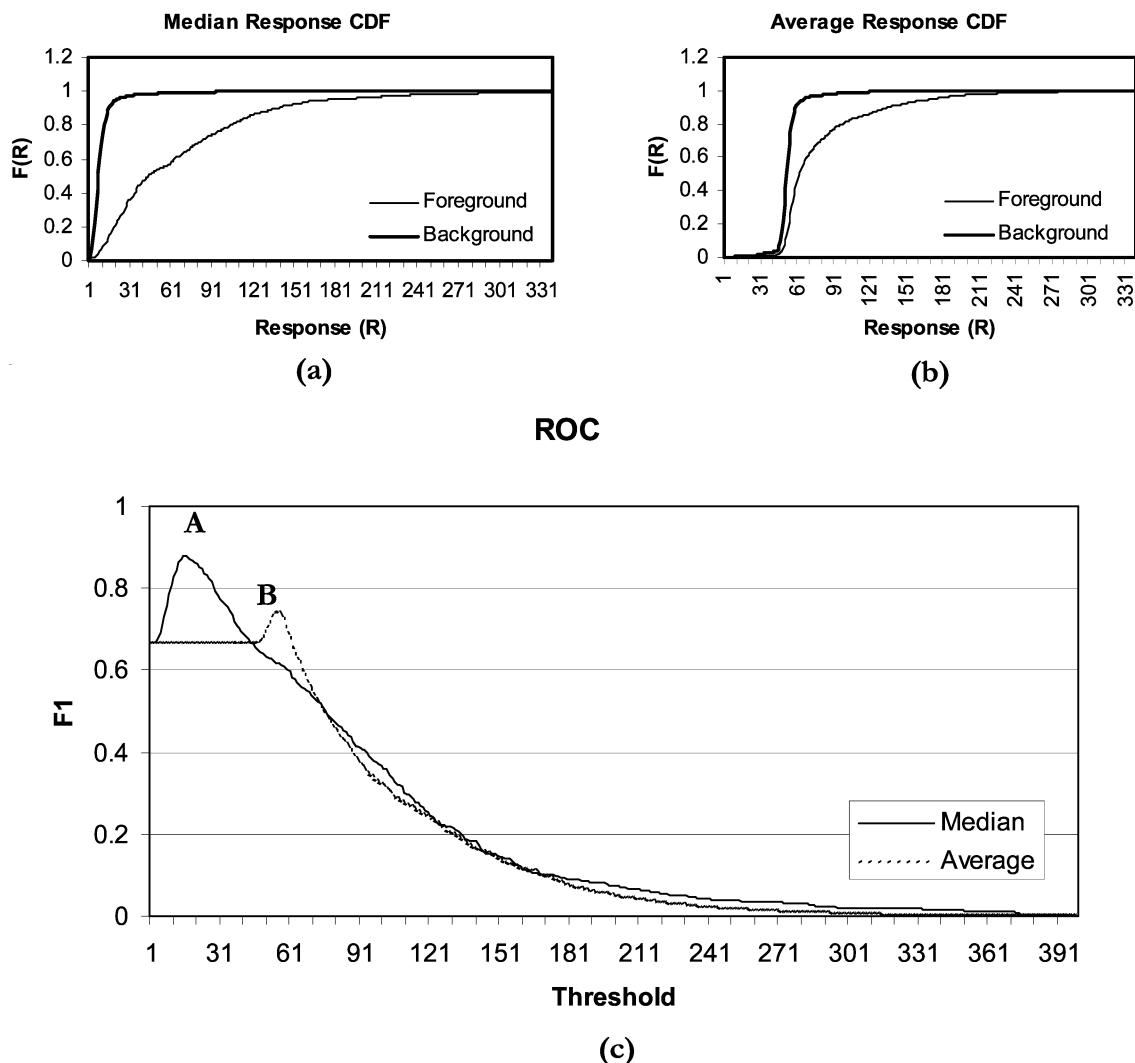
Fig. 5. Illustrating the superiority of the median template response compared to the average template response for a low magnification image. The responses are computed at true boundary points (i.e., foreground) and at randomly selected background points (i.e., background) (a) CDF of the median response. (b) CDF of the average response. Clearly, the median response is better at separating foreground and background points than the average response. For the median response the Kolmogorov–Smirnov (K–S) value is 0.76 (obtained at $R = 15$), and for the average response the K-S value is 0.5 (obtained at $R = 57$). (c) The ROC curves for the same low contrast image. The point A is the best operating point on the median response curve and is obtained at a threshold value of 15, with $F_1 = 88.1\%$, $R = 87.3\%$, and $P = 88.9\%$. The point B is the best operating point on the average response curve and is obtained at a threshold value of 54, with $F_1 = 74.8\%$, $R = 78.8\%$, and $P = 71.2\%$.

referred to as outliers in statistical terms. Although pixel intensities can only assume positive values, the response of a LPD can be either negative or positive, resulting in arbitrarily high or low responses when corrupted with outliers. Hence, a false background response can be confused with a boundary template response, and vice versa. Similar to median filters used in image processing, we can redefine the template responses (1) by computing a median rather than mean for the LPD kernels along the edge direction as follows:

$$R(\boldsymbol{p}, \boldsymbol{u}) = \operatorname*{median}_{j=1\ldots K}(\boldsymbol{p} + \mathrm{j}\boldsymbol{u}, \boldsymbol{u}_\perp). \qquad (4)$$

The length K is estimated analogous to the average response based tracing algorithm described in [13]. The robustness of the median template response for different situations is illustrated by an example in Fig. 4. Note that the median response

measure holds while up to 50% of the LPD responses are corrupted. Hence any stopping criteria defined based on template responses can more accurately detect the neurons from the false background responses. The situations where using the median response is advantageous are:

1) Broken/Discontinuous Segments: The median-based algorithm can jump over missing structures, whereas the average based algorithm terminates prematurely [see Fig. 4(a)], especially in low-SNR and low-magnification images where the neurons are thinner and therefore more vulnerable to noise.
2) Discontinuous Boundaries: The continuity of the boundaries is violated by thin structures, possible branches or undesired structures in the image [see Fig. 4(b)]. These structures cause the average based template tracing to stop prematurely, but the median based template is robust to
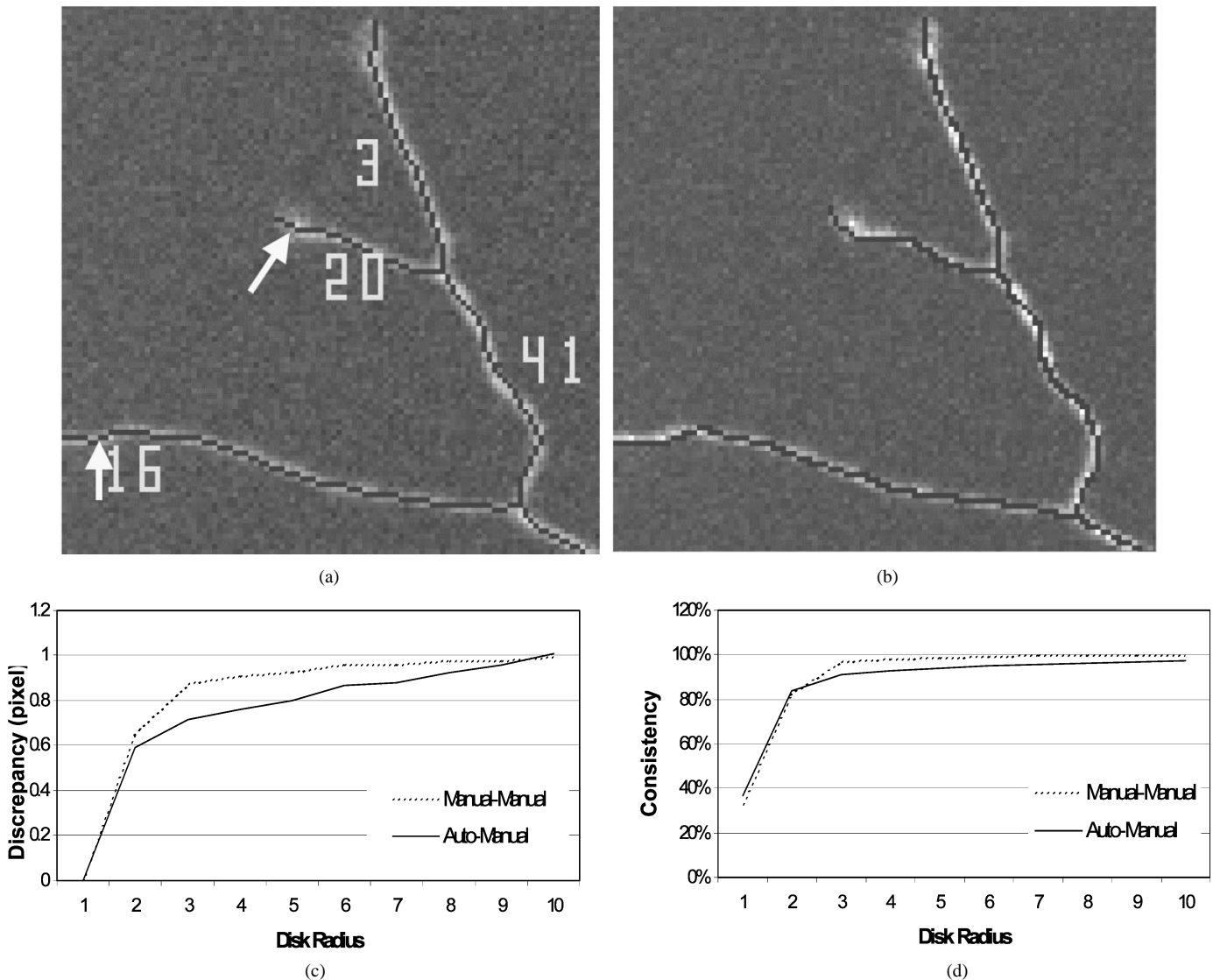
Fig. 6.   Comparing the quality of the automatic and manual traces. (a) A portion of an automatic trace magnified 5 times. (b) Manual trace of the same region. In general, automatic traces are smoother than manual traces. The arrows highlight a few such differences. (c-d) Comparing the inconsistencies between automatic and manual traces (A-M), with those between two sets of manual traces (M-M) for the same neuron image. Discrepancy (μ) and consistency are plotted as a function of disk size in Panels (c) and (d), respectively. Observe that the (A-M) average error is smaller than the (M-M) average errors.

such artifacts as long as the width of such distortions is less than half of the template length.

3) Impulsive Noise: The median response is robust to impulsive noise, as long as half of the data is not corrupted [see Fig. 4(c)].

4) Curvature: Unlike the mean based algorithm, the median based tracing is less prone to premature stopping in regions of high curvature [see Fig. 4(d)] significantly improving the results particularly for low-resolution images where the curvature is higher.

Note that, other than replacing the average response with the median response, the tracing algorithm introduced in the previous section and discussed in detail in [8], [13] remains the same. The next section illustrates the superiority of the median template response over the average response, especially in images with low SNR.

V. MEDIAN VS. AVERAGE; AN EMPIRICAL STUDY

The following experiment illustrates the superiority of the median template response over the average response. A total of 6 images were traced manually. For each image, the templates were applied at each of its known boundary points, and the responses were histogrammed. To compensate for the fact that manual traces may not exactly coincide with the true boundary points, templates were applied at points adjacent to boundary points in several directions and maximum responses were noted. This resulted in two response histograms per image, one containing average template responses, and the other containing median template responses. Similarly, two background response histograms were generated per image by applying the templates at randomly selected background points. At each background point, the templates were allowed to shift (move) and rotate locally, for maximum median and average template

(a)

(b)

(c)

(d)

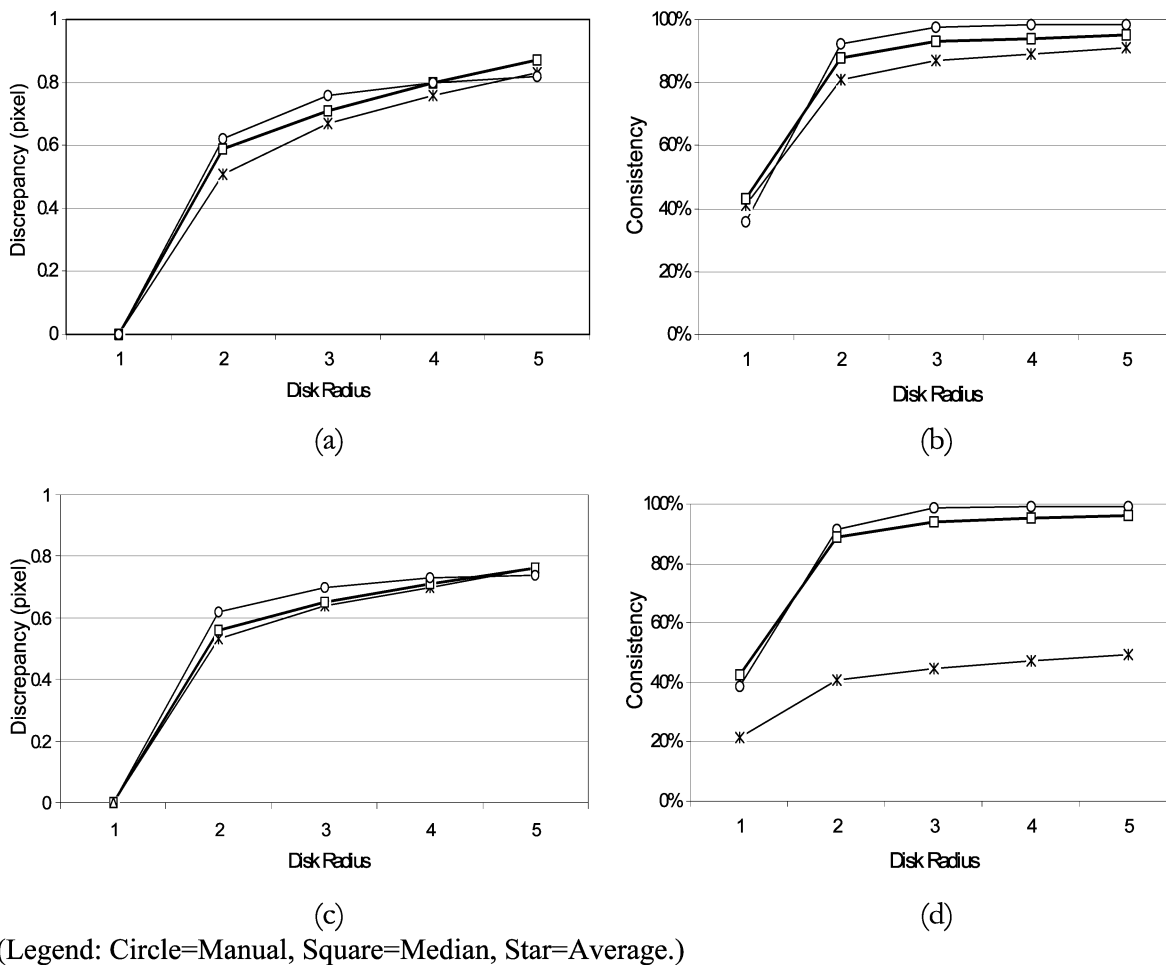(Legend: Circle=Manual, Square=Median, Star=Average.)

Fig. 7. Illustrates the discrepancy (average error of corresponding traces) and the consistency (percentage of inliers) as a function of disk radius δ. (a)–(b) High-contrast images. (c)–(d) Low-contrast images. Observe that the manual traces are superior to the automatic ones in both image types for most values of $\delta > 1$. Median based tracing is more consistent and has less error than average based tracing. This improvement is significant for low-contrast images.

responses. The foreground and background histograms of a particular image contain the same number of points. Fig. 5 illustrates the foreground and background accumulative normalized histograms [which are estimates of the corresponding cumulative distribution functions (cdf)] for a sample low-contrast image. Observe that the foreground and background median cdf's in Fig. 5(a) are more separated than the CDF's for the average responses illustrated in Fig. 5(b). Quantitatively this can be measured using the Kolmogorov-Simirov (K-S) test, which measures the maximum difference between the two cdf's. The median response definition resulted in a K-S measure of 0.76 while the average response resulted in a K-S measure of 0.57. Higher K-S values imply that responses at true boundary points are separable from responses due to background irregularities and noise. For instance, one can compare the performance of the two response estimators by applying a varying threshold to the histograms and at each threshold compute the classification error.

Let TP denote the number of *true positives*, i.e., the number of foreground points that passed the threshold. Let FN be the number of *false negatives*, i.e., the number of foreground points that did not pass the threshold. Let TN be the number of *true*

negatives, i.e., the number of background points that did not pass the threshold. Let FP be the number of *false positives*, i.e., the number of background points that passed the threshold. We define the *recall*, R, and *precision*, P, according to

$$R = \frac{TP}{TP + FN}; \qquad (5)$$

$$P = \frac{TP}{TP + FP}. \qquad (6)$$

Ideally, a template should produce positive responses over the foreground, and zero responses over the background. In such an ideal situation, one can perfectly classify foreground and background points. Therefore, achieving recall and precision of 100%. In real images, however, such situations rarely occur, and a balance between precision and recall should be achieved. To compare the performance of the two template responses, it is more convenient to use a single measure instead of two. One of the most frequently used measures combining both recall and precision is the F measure, which is defined as

$$F = \frac{(1 + \beta)RP}{\beta R + P} \qquad (7)$$

TABLE I
LISTING OF THE α_{iG} AND THE α_{Gi} VALUES FOR LOW- AND HIGH-CONTRAST IMAGES

Disk Radius	High-Contrast Images				Low-Contrast Images			
	Recall α_{Gi}		Precision α_{iG}		Recall α_{Gi}		Precision α_{iG}	
	Average	Median	Average	Median	Average	Median	Average	Median
1	0.41	0.43	0.34	0.35	0.22	0.42	0.41	0.33
2	0.81	0.88	0.70	0.73	0.41	0.89	0.79	0.74
3	0.87	0.93	0.76	0.77	0.45	0.94	0.88	0.81
4	0.89	0.94	0.77	0.79	0.47	0.95	0.91	0.83
5	0.91	0.95	0.79	0.80	0.49	0.96	0.94	0.85

where β, a weighting factor, determines the relative weight of the recall and precision components, depending on the application. For the following experiments, β was set to 1, i.e., the recall and precision were assigned equal weights. The resulting measure is often called the F_1 measure. F_1 curves are the receiver operating characteristics (ROC) curves used in detection theory.

Applying a varying threshold to the cdf's of Fig. 5(a) and (b) produced the F_1 curves in Fig. 5(c). The best operating point using the median response definition was obtained at a threshold of 15, and corresponds to a F_1 value of 88.1%, ($R = 87.3\%$, and $P = 89.3\%$). This is denoted by A in Fig. 5(c). Compare this with the best operating point using the average response definition denoted by B and corresponds to $F_1 = 74.8\%$, ($R = 78.8\%$, and $P = 71.2\%$). The results obtained from the other images suggest a similar conclusion—that the median response is clearly superior to the mean.

For completeness, we compared the two algorithms on a typical high contrast, high SNR image. Similar to the above result, the cdf's of the median responses were found to be more separable than the cdf's of the average responses. However, the differences are not as substantial as those observed for low SNR. Quantitatively, the estimated K-S measures were 0.84 for the median and 0.79 for the average, resulting in a K-S difference of 0.05. Compare this with a difference of 0.19 (i.e., 0.76–0.57) for the low SNR image of Fig. 2. The same conclusion can be reached by comparing the best operating point from the ROC curves for both images. To summarize, the median outperforms the average regardless of image type. However, the median outperforms the average by a much larger margin in low contrast images. This conclusion is supported by hundreds of traces of actual neuron images.

This section has illustrated that the median template response is superior to the average template response with respect to classifying foreground and background points. However, it is necessary to analyze the effect of the two response definitions on the accuracy of the tracing algorithms. This will be considered in detail in Section VII in the context of a validation study.

VI. EXPERIMENTAL RESULTS

This section describes the specimen preparation, imaging protocols, computational setup, and presents some sample results. The tracing algorithms presented in this work have been implemented and are in use since April 1999 at Wadsworth Research Laboratory of the New York State Health Department, Albany, NY. The images presented here are merely samples that were selected to illustrate certain aspects of the algorithms.

A. Specimen Preparation and Imaging Protocols

The neurons were obtained from whole brains from several embryonic (day 18) Sprague–Dawley rats. The brains were dissected, pooled, and maintained on ice in Hepes buffered saline solution (BSS) supplemented with 100 U/ml penicillin and 100 U/ml streptomycin [41]. Under a dissecting microscope, hippocampi were dissected, cleaned of meningeal tissue, collected, then enzymatically digested with a solution of 2.5-mg/ml trypsin in BSS at 37 °C, without shaking, for 15 min. Digested tissue was rinsed three times with BSS at room temperature (five minutes per rinse) and mechanically dissociated by repeated pipetting first with a Pasteur pipette, and then with a Pasteur pipette that had been fire polished to reduce the internal diameter by one half. Dissociated neurons were then seeded directly onto poly-lysine coated coverslips or silicon colonnade surfaces at a density of 2.6×10^3 cells/cm² and allowed to adhere for two hours.

The surfaces with adherent neurons were inverted and submerged in glial-conditioned N2.1 media so that adherent neurons were facing, but separated from, a layer of previously prepared astrocytes. The resultant inverted cocultures were maintained for 24 hours under standard cell culture conditions. The adherent neurons were rinsed with HBHS and fixed in situ using warm (37 °C) 4% paraformaldehyde for 10 minutes.

Fixed neurons were treated in 1% triton X-100 in HBHS at room temperature for 10 minutes and then in 6% BSA in HBHS

TABLE II
LISTING OF THE F_1 VALUES FOR THE TEN HIGH CONTRAST IMAGES AND THE FIVE LOW CONTRAST
IMAGES COMPUTED USING THE AVERAGE AND THE MEDIAN TRACING ALGORITHMS

Image Number	High-Contrast Images		Low-Contrast Images	
	Average	Median	Average	Median
1	0.88	0.91	0.89	0.88
2	0.81	0.84	0.87	0.87
3	0.88	0.90	0.43	0.86
4	0.93	0.94	0.72	0.84
5	0.87	0.91	0.59	0.87
6	0.85	0.89		
7	0.81	0.83		
8	0.81	0.81		
9	0.85	0.87		
10	0.86	0.88		
Overall Average	0.855	0.878	0.70	0.864

for 30 minutes. The neurons were labeled using a solution containing an antibody to a neuron specific subunit of tubulin (clone TuJ1, diluted 1:500, BabCO) in HBHS at 37 °C for 1 hour. The neurons were then incubated in a biotin conjugated anti-mouse antibody (diluted 1:200, Sigma) or in Alexa-488 conjugated antibody (diluted 1:200, Molecular Probes, Eugene, OR) at 37 °C for 40 min. Neurons stained using the biotinylated antibody were subsequently stained with Quantum Red-conjugated streptavidin (diluted 1:50, Sigma) in HBHS at room temperature for 30 minutes. All samples were rinsed in HBHS and mounted on coverslips in a 1:1 (v/v) solution of glycerol (Sigma): HBHS supplemented with 1% n-propyl gallate.

All fluorescently labeled samples were imaged by scanning laser confocal microscopy using either a BioRad MRC 600 or a NORAN OZ confocal unit attached to an Olympus inverted microscope using a 10X 0.40 numerical aperture objective lens. Each x, y image was recorded as a single frame to minimize photodamage. This results in noisy images compared to integrated images recorded either by slower scanning or signal integration of multiple scans. An additional issue is the possibility of nonuniform fluorophore absorpotion that results in apparent discontinuities.

The tracing program is implemented in C++ and does not require any special hardware. The results here were obtained using a Pentium III 500-MHz PC, with 128 Mbytes of RAM. A typical $768 \times 512 \times 8$ image is processed in less than 5 s. This includes I/O, soma detection, tracing, and presentation. The actual tracing time depends on the complexity of the image, but is usually around one second.

Eight images were selected mostly at random, however, some were selected to illustrate certain aspects of the algorithms. All images are gray scale with 8 bits/pixel. None of the images were manipulated before processing. However, in all instances, image contrast and brightness were manipulated *after* they have been traced by our algorithm for printing purposes (many structures were too dim for direct printing). In other words, the algorithms used the raw data.

Fig. 1 illustrates an image and the corresponding traces. The image has the dimensions 768×512 pixels. Segments and somas are labeled with numbers and letters, respectively, while intersection/bifurcation points are marked with cross hairs. The program uses two-letter codes (e.g., "AA", "AB", etc.) for soma identification. In addition to the traces, the program generates two text outputs. The first is a text representation of the somas and the traces in a format compatible with the Neurolucida software (MicroBrightfield Inc., Williston, VT). The second output is a text summarization of neuronal structures found in an image. Fig. 2 illustrates a low SNR image along with its average and median generated traces.

A quantitative analysis of the tracing algorithm is presented in the next section. However, a few observations are in order. First, the tracing algorithm appears to be robust against nonuniform backgrounds, as illustrated by Fig. 2. Second, neither the tracing nor the soma detection algorithms were affected by the high intensity regions surrounding the somas in the images. Third, tracing seems to terminate prematurely occasionally which can be corrected by adjusting certain parameters in the tracing algorithm. However, we were unable to identify a single parameter
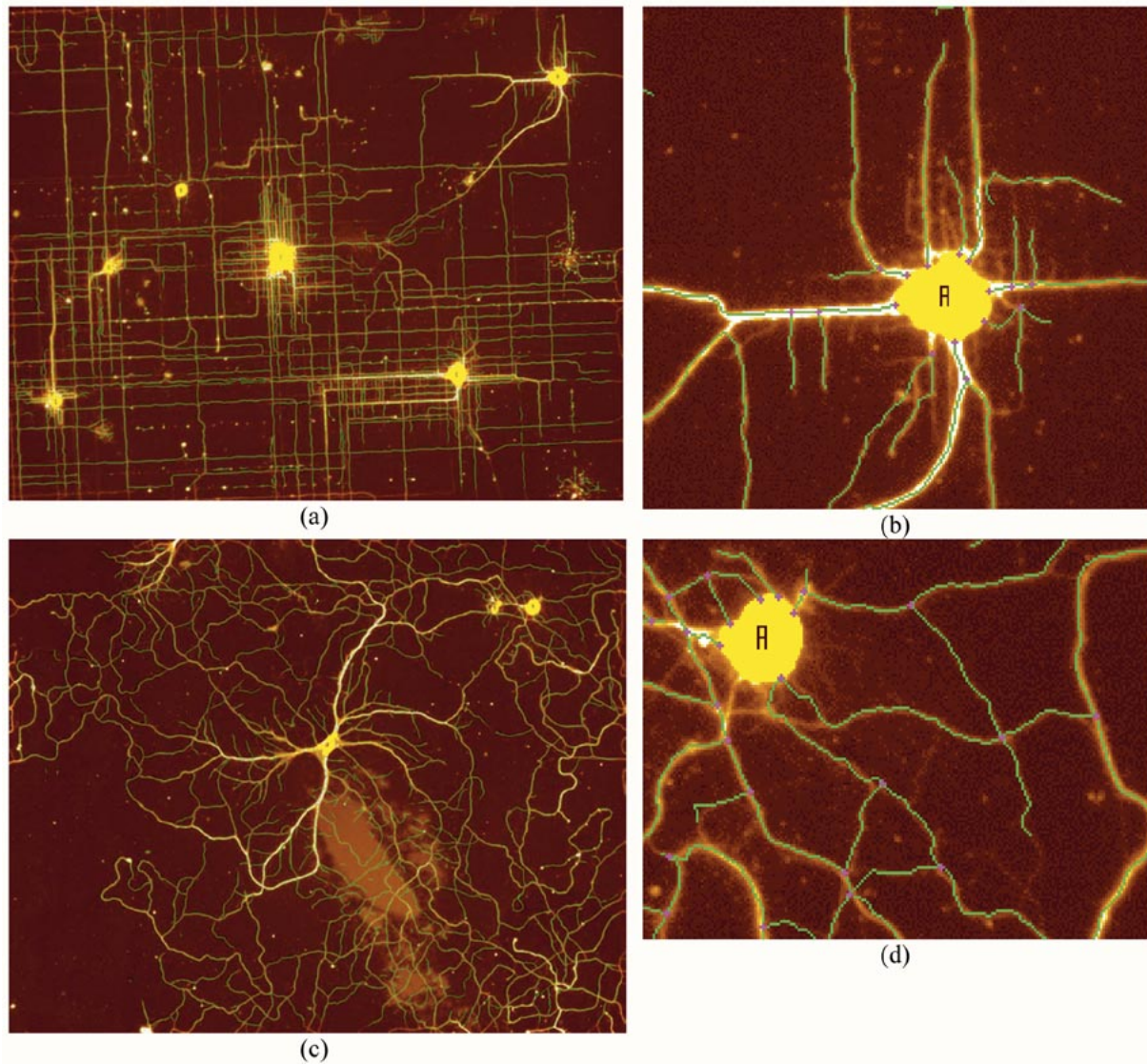
Fig. 8.   Further examples from a large-scale study [48] of neuronal behavior on patterned surfaces. Panel (a) is the result of automatically tracing a 1280×1024 pixel image of neurons grown over a micropillar array with pillar width of $2\,\mu$m, and spacing of $1.5\,\mu$m. Panel (b) is an enlarged view of the trace around the neuron at the upper right portion of the image. The traces are shown in green and the tips/junctions are shown in purple. The image is displayed using a heated-object color scale that best highlights the background detail for this data. Panels (c) and (d) correspond to a smooth etched surface. The neurons grow much more randomly in this case.

that can generalize over all types of images, hence none of the program parameters were adjusted manually.

VII. METHODS FOR VALIDATING THE TRACING ALGORITHMS

This section presents a validation study of the tracing algorithm. This includes validating the accuracy as well as the consistency of the algorithms. Accuracy is estimated with respect to a ground truth. Consequently, methods for establishing the ground truth for 2-D neuron images from a set of manual traces are presented. Since the ground truth is an estimate calculated from manually traced images, we prefer to use the terms "discrepancy" and "consistency" rather than "localization" and "detection." Quantitative measures for estimating the similarity between sets of traces, and between traces and the corresponding ground truth are also presented.

The discrepancy of the tracing algorithms is quantitatively measured with respect to the estimated ground truth. It is measured in pixels, and represents the error between the program-generated traces and the manual ones. The consistency of the tracing algorithms, on the other hand, measures the ability of the algorithms to regenerate traces after introducing certain types of image variations. It is the percentage of the common traces detected; hence it will be quantified in terms of the similarity between the two sets of traces.

From a neuroscientist's point of view, several structural characteristics of neurons are important. These include soma centroids, volumes, surface areas, and connectivity with other somas. In addition, it is important to determine the centerlines of all dendritic/axonal structures, their lengths, surface areas and volumes. It is also of interest to determine the topology of such structures. For instance, one parameter of particular

interest is the order of a segment in the tree-like neuronal structure. Indeed, it is known that first-order (i.e., primary dendrites emerging from the soma) have different electrical properties compared to higher-order segments.

Clearly, quantitative evaluation of an automatic system based on these characteristics requires the availability of ground truth, or a suitable "Gold Standard." In the context of neuron images, the ground truth has to be established manually. It is usually difficult for a human to manually generate accurate and consistent traces. As illustrated in Fig. 6(a-b), manual traces are often jerky and don't line-up with the structures' true centerlines. Furthermore, manual traces often suffer from inter- and intraexpert variability. Manual traces of the same image generated by different human experts or by the same expert but at different times do not coincide exactly. In fact, we will illustrate that automatic traces are superior to manual traces as far as the location of the centerline points is concerned. Hence, in this context, it is inappropriate to validate the automatically generated centerlines against their manual counterparts. On the other hand, the human observer is better at detection of segments. If the objective of a validation study is to determine whether there is a one-to-one correspondence between automatically generated traces and dendritic structures (i.e. detection-rate vs. false-alarm rate, or the average number of false positives and false negatives in a given image), then one would expect manual tracing to be superior to its automatic counterpart.

A. Algorithms for Measuring the Similarity of Traces

This section introduces methods to quantitatively measure the similarity between two sets of traces corresponding to the same neuron image. The measures are based on the Euclidean distances between the corresponding traces. The discrepancy between two sets of centerline points is measured by computing the average Euclidean distance between the points that are within a distance δ. The consistency between two sets is measured by finding the percentage of points that are within a distance of δ.

Let the neural structure centerline location sets from the two images be denoted $\mathbf{P}$ and $\mathbf{Q}$ with $|\mathbf{P}|$ and $|\mathbf{Q}|$ points respectively. Let the subset $\mathbf{P}_q \subseteq \mathbf{P}$ be the inlier points that have a correspondence in the other image; in other words for each point $\mathbf{p} \in \mathbf{P}_q$ there exists a point in $\mathbf{q} \in \mathbf{Q}$ such that the Euclidean distance between these two points is less than a δ. Furthermore, denote the corresponding point of $\mathbf{p} \in \mathbf{P}_q$ in the set $\mathbf{Q}$ by $\mathbf{C}_q(\mathbf{p}) = \arg\min_{\mathbf{q} \in \mathbf{Q}} \|\mathbf{p} - \mathbf{q}\|$. Similarly, let $\mathbf{Q}_p \subseteq \mathbf{Q}$ denote the subset of inlier points in $\mathbf{Q}$ whose closest point in set $\mathbf{P}$ is less than δ, and for each $\mathbf{q} \in \mathbf{Q}_p$ let $\mathbf{C}_\mathbf{P}(\mathbf{q})$ denote its correspondence in set $\mathbf{P}$.

Observe that the number of points in $\mathbf{P}_q$ is not necessarily equal to the number of points in $\mathbf{Q}_p$, because one-to-one correspondence is not enforced due to the curved nature of the traces. The spatial discrepancy between the two traces is defined by

$$\mu = \frac{1}{2|\mathbf{P}_q|} \sum_{\mathbf{p} \in \mathbf{P}_q} \|\mathbf{p} - \mathbf{C}_q(\mathbf{p})\| + \frac{1}{2|\mathbf{Q}_p|} \sum_{\mathbf{q} \in \mathbf{Q}_p} \|\mathbf{q} - \mathbf{C}_\mathbf{P}(\mathbf{q})\|.$$

$$(8)$$

The consistency between the two traces are defined by

$$\alpha_{pq} = \frac{|\mathbf{P}_q|}{|\mathbf{P}|} \times 100\%; \qquad (9\text{-a})$$

$$\alpha_{qp} = \frac{|\mathbf{Q}_p|}{|\mathbf{Q}|} \times 100\%. \qquad (9\text{-b})$$

Observe that the two consistency measures, while similar in definition, may have different meaning as will be explained shortly. Exhaustive search is required to establish correspondences between sets of tracing points. However, this can be accomplished efficiently using Euclidean Distance Maps.

B. Comparison of Manual and Automatic Traces—A Case Study

Twenty-one neuron images were manually traced at least once. Five images were traced five times by the same person, but during different sessions. The images were then traced using the tracing algorithm running in a batch mode (i.e., no tracing parameters were adjusted). Manual and automatic traces of an image are cropped and enlarged for comparison and illustrated in Fig. 6(a) and (b). The traces are very similar, but this needs to be established quantitatively. Fig. 6(c) and (d) illustrates the average discrepancy μ and the consistency α_{MA} between a manual trace ($\mathbf{M}$) and an automatic trace ($\mathbf{A}$) for the complete image of Fig. 6(a) and (b). Fig. 6(c) illustrates that the discrepancy between the two manual-traces are larger than those between a manual trace and an automatic trace. For example, for $\delta = 3$, the discrepancy (average error) between the two manual traces is 0.88 pixels, while the discrepancy between an automatic trace and the manual traces is 0.72 pixels. Although the difference between these two sets of traces is not large especially when taking digitization errors into account, still it illustrates the quality of automatic traces. Fig. 6(d) illustrates that the consistency between automatic and manual traces is slightly less than those measured between two sets of manual traces. For example, at $\delta = 3$, 97% of the points in the two manual traces were found to be inliers to each other, while only 91% of the points in the automatic trace were found to be inliers to their manual counterparts. This is expected, because humans are less likely to skip available structures or trace background noise.

The same observations were found to be true for all other sets of manual and automatic traces. This leads us to conclude that automatic traces are, at the very least, of comparable quality to manual ones as far as locating the true location of the centerlines are concerned. Because of the observed discrepancy between sets of manual traces, one can conclude that no single manual trace is a good estimate of the true centerline. To quantitatively measure the accuracy of the automatic tracing algorithm, we first establish the true location of the centerlines (i.e., ground truth) and then measure the discrepancy relative to the established ground truth. This is described next.

C. Methods for Approximating the Ground Truth

For the purposes of this work, the true location of the centerlines is approximated for ten high-contrast images and five low-contrast images. Each image was traced five times, by different people, or by the same person at different times. There-

fore, resulting in 75 manual traces. Furthermore, both the average and the median tracing algorithms were used to trace all images. Therefore, resulting in a total of 105 images (traces). To establish the ground truth for a given image, we first established correspondences between all of its manual traces. Ideally, the true location of centerline points would be estimated by the average of each of the correspondence sets. However, this may result in discontinuities in the estimated ground truth. Alternatively, the following algorithm approximates averaging and produces continuous centerlines. First, we superimpose the manual traces on an image, with pixel intensities being a function of the number of matching traces. Then perform a morphological closing using a 3×3 structuring element of the form $\begin{bmatrix} 1 & 1 & 1 \\ 1 & 1 & 1 \\ 1 & 1 & 1 \end{bmatrix}$ to produce hole-free centerlines. Finally, we apply a modified version of the sequential thinning algorithm described in [42] to estimate the true location of the centerlines.

Notice that without the above closing operation the ground truth centerlines may contain holes (i.e., a fork in the centerline followed by a merge). Clearly, this is not desirable because we would like the ground truth to be representative of the manual traces collectively, not individually. The closing operation has another desirable effect. Notice that the above structuring element results in images where pixel intensities are directly proportional to the number of manual traces contributing to them. This is desirable because the thinning algorithm is designed to remove low intensity pixels before high intensity ones, which means centerlines that agree with the majority of traces at each point.

D. Quantitative Analysis of the Tracing Algorithms

In this section, we use ground truth estimates to show that 1) manual traces are superior to automatic traces with respect to tracing all segments present, and avoiding background noise, 2) automatic traces are more accurate than manual traces in estimating the true location of the centerline pixels, and 3) the median tracing algorithm is superior to the average tracing algorithm, especially in low-quality images.

Manual Versus Automatic: First we compare manual traces and automatic traces against the ground truth with respect to the percentage of inliers at different disk sizes. This is illustrated in Fig. 7(b) for high-contrast images and in Fig. 7(d) for low-contrast images. For instance, the curve corresponding to the manual traces in Fig. 7(b) was generated by 1) computing the percentage of inliers points of each of the manual traces with respect to the ground truth, α_{Gi}, and 2) taking the average over all traces at each disk radius value, δ. Clearly, the manual traces are superior to the automatic traces in both low- and high-contrast images, with the average-tracing algorithm being much worst for the low-contrast images. This is because human tracers are less likely to trace the background (i.e., overtrace) or miss entire or parts of segments (i.e., under-trace), and the ground truth itself is established by manual traces. Therefore, *we conclude that manual traces are superior in detecting more segments and avoiding background traces*. However, this does not mean that manual traces are more accurate, in other words that they have low discrepancy. This is because accuracy is a function of error

between the true location of a point and its estimated one as measured by the discrepancy μ. In fact, if we only consider inlier points (i.e., those points having corresponding ground truth points), then the average tracing algorithm was found to be the most accurate. This is illustrated in Fig. 7(a) and (c). The fact that the average tracing algorithm was found to be slightly more accurate than the median can be attributed to the fact that the Euclidean distance is the error measure minimized by the mean statistics for the inlier points.

Median Versus Average: Recall that α_{iG} represents the percentage of points in the traces i that are inliers to ground truth points, while α_{Gi} represents the percentage of points in the ground truth that are inliers to points in the traces i. In other words, α_{iG} is a measure of *precision* while α_{Gi} is a measure of *recall*. Table I lists some of these values for low- and high-contrast images. For example, from the row $\delta = 2$ in the high-contrast images, Observe that 81% of the points generated by the average tracing program are adjacent to true centerline points. Compare this with 88% for the median algorithm. Furthermore, 70% and 73% of the points in the ground truth were adjacent to points generated by the average- and median-tracing programs, respectively. The difference is more significant in low-contrast images. For example, the row $\delta = 2$ in the low-contrast images column indicates that the average tracing algorithm has a precision of 41%, while the median has a precision of 89%. On the other hand, the average tracing algorithm has slightly better recall than the median at 79% and 74%, respectively. In other words, although the average tracing algorithm was able to trace 79% of the segments present in the image, 59% of the traces it generated correspond to background noise rather than actual segments. This is consistent with our earlier statement that the average tracing algorithm tends to over-generate.

To compare the performance of the average and median tracing algorithms against each other, we assume that both α_{iG} (i.e., precision) and α_{Gi} (i.e., recall), are equally important and compute the F_1 measure for the average and median traces. In terms of the recall and precision estimates, the F_1 measure defined in (7) can be rewritten as

$$F_1 = \frac{2\alpha_{iG}\,\alpha_{Gi}}{\alpha_{iG} + \alpha_{Gi}}. \tag{10}$$

This allows us to calculate the F_1 (ROC) curves for each image as a function of the inlier distance threshold δ. The F_1 values obtained using $\delta = 3$ are listed in Table II for the ten high contrast images as well as the five low contrast images. Table II clearly illustrates the superiority of the median tracing algorithm over the average algorithm, especially in low contrast images. This is clearly illustrated by the last row in Table II, which lists the average F_1 values obtained over all high- and low-contrast images.

VIII. SUMMARY AND CONCLUSIONS

In this work, we have presented fully automatic algorithms for tracing of neurons from digital images. The algorithms are fast, hence they are appropriate for large scale applications. They are also accurate and robust against image artifacts such as low contrast, and apparent discontinuities and/or hollowness of structures. This work extends our earlier work [8], [13]

by presenting the median kernel response, a view of kernel responses that is different from the traditional correlation-like views. The superiority of this new kernel-response method was established quantitatively using ROC-like curves and is supported by our results [48] obtained from thousands of images.[1] Some examples are shown in Fig. 8. This new and novel view of kernel-responses may prove useful in other kernel-based tracing algorithms. We have also presented a set of methods for establishing ground truth and for validating the tracing algorithms.

The median-based tracing requires a slightly higher computational cost than the average-based tracing, but the algorithm are still fast enough for the applications of interest, since only a fraction of a second is added to the computing times. Overall, the median-based algorithm is still much faster compared to manual tracing. The robustness and efficiency of the proposed method makes it attractive for large-scale applications such as high-throughput assays, and the Human Brain Project [43]. They are especially valuable when live specimens are being imaged. An application of direct interest to us is the detection and quantification of morphological changes caused by a variety of biochemical and physiological agents, disease and trauma. Also of interest are attempts to simulate computationally the electro-chemical behavior of large collections of neurons [44] for which actual, rather than simulated, neuro-anatomical data, would be valuable.

In our earlier work [13] we presented algorithms for tracing neurons in 3-D volumetric images. Currently, we are extending the median-based tracing method described here to 3-D images of neurons and tumor vasculature in support of angiogenesis studies.

ACKNOWLEDGMENT

REFERENCES

[1] J. J. Capowski, Ed., *Computer Techniques in Neuroanatomy*. New York: Plenum, 1989.
[2] J. D. Clements and S. J. Redman, "Cable properties of cat spinal motoneurons measured by combining voltage clamp, current clamp and intracellular staining," *J. Physiol.*, vol. 409, pp. 63–87, 1989.
[3] S. Cullheim, J. W. Fleshman, L. L. Glenn, and R. E. Burke, "Membrane area and dendritic structure in type-identified triceps surae alpha motoneurons," *J. Comp. Neurol.*, vol. 255, pp. 68–81, 1987.
[4] B. Ulfhake and J. O. Kellerth, "Electrophysiological and morphological measurements in cat gastrocnemius and soleus—motoneurons," *Brain Res.*, vol. 307, pp. 167–179, 1984.
[5] B. Ulfhake and S. Cullheim, "A quantitative light microscopic study of the dendrites of cat spinal α-motoneurons after intracellular staining with horseradish peroxidase," *J. Comp. Neurol.*, vol. 202, pp. 585–596, 1981.
[6] G. Simic, I. Kostovic, B. Winblad, and N. Bogdanovic, "Volume and neuron numbers of the human hippocampal formation in normal aging and Alzheimer's disease," *J. Comp. Neurol.*, vol. 379, pp. 482–494, 1997.
[7] I. Liu and Y. Sun, "Recursive tracking of vascular networks in angiograms based on detection-deletion scheme," *IEEE Trans. Med. Imag.*, vol. 12, pp. 334–341, June 1993.
[8] A. Can, H. Shen, J. N. Turner, H. L. Tanenbaum, and B. Rosyam, "Rapid automated tracing and feature extraction from retinal fundus images using direct exploratory algorithms," *IEEE Trans. Inform. Technol. Biomed.*, vol. 3, no. 2, pp. 125–138, June 1999.
[9] Y. Sun, R. J. Lucariello, and S. A. Chiaramida, "Directional low-pass filtering for improved accuracy and reproducibility of stenosis quantification in coronary arteriograms," *IEEE Trans. Med. Imag.*, vol. 14, no. 2, pp. 242–248, June 1995.
[10] J. R. Glaser and E. Glaser, "Neuron imaging with neurolucida—a PC-based system for image combining microscopy," *Comput. Med. Imag. Graph.*, vol. 14, pp. 307–317, 1990.
[11] C. F. Garvey, J. Young, W. Simon, and P. D. Coleman, "Automated three-dimensional dendrite tracking system," *Electroencephalogr. Clin. Neurophysiol.*, vol. 35, pp. 199–204, 1973.
[12] P. D. Coleman, C. F. Garvey, J. Young, and W. Simon, "Semiautomatic tracing of neuronal processes," in *Computer Analysis of Neuronal Structures*, R. D. Lindsay, Ed. New York: Plenum, 1977, pp. 91–109.
[13] K. Al-Kofahi, L. Lasek, D. Szarowski, C. Pace, G. Nagy, J. N. Turner, and B. Roysam, "Rapid automated three-dimensional tracing of neurons from confocal image stacks," *IEEE Trans. Inform. Technol. Biomed.*, vol. 6, June 2002.
[14] A. R. Cohen, B. Roysam, and J. N. Turner, "Automated tracing and volume measurements of neurons from 3-D confocal fluorescence microscopy data," *J. Microscopy*, pt. 2, vol. 173, pp. 103–114, Feb. 1994.
[15] M. H. Goldbaum, N. Katz, S. Chaudhuri, M. Nelson, and P. Kube, "Digital image processing for ocular fundus images," *Ophthalmol. Clin. North Amer.*, vol. 3, no. 3, pp. 447–466, Sept. 1990.
[16] M. H. Goldbaum, V. Kouznetsova, B. L. Cote', W. E. Hart, and M. Nelson, "Automated registration of digital ocular fundus images for comparison of lesions," *SPIE: Ophthalmic Technologies III*, vol. 1877, pp. 94–99, 1993.
[17] T. M. Clark, W. R. Freeman, and M. H. Goldbaum, "Digital overlay of fluorescein angiograms and fundus images for treatment of subretinal neovascularization," *Retina- J. Retinal and Vitreous Diseases*, vol. 2, no. 12, pp. 118–126, 1992.
[18] S. Chaudhuri, S. Chatterjee, N. Katz, M. Nelson, and M. Goldbaum, "Detection of blood vessels in retinal images using two-dimensional matched filters," *IEEE Trans. Med. Imag.*, vol. 8, pp. 263–269, 1989.
[19] M. Sonka, M. D. Winniford, and S. M. Collins, "Reduction of failure rates in automated analysis of difficult images: improved simultaneous detection of left and right coronary borders," *Comput. Cardiol.*, pp. 111–114, 1992.
[20] M. Sonka, M. D. Winniford, X. Zhang, and S. M. Collins, "Lumen centerline detection in complex coronary angiograms," *IEEE Trans. Biomed. Imag.*, vol. 41, pp. 520–528, 1994.
[21] M. Sonka, M. D. Winniford, and S. M. Collins, "Coronary borders in complex images," *IEEE Trans. Med. Imag.*, vol. 14, pp. 151–161, 1995.
[22] P. H. Eichel, E. J. Delp, K. Koral, and A. J. Buda, "A method for a fully automatic definition of coronary arterial edges from cineangiograms," *IEEE Trans. Med. Imag.*, vol. 7, no. 4, pp. 313–320, 1988.
[23] M. A. Figueiredo and M. N. Leitao, "A nonsmoothing approach to estimation of vessel contours in angiograms," *IEEE Trans. Med. Imag.*, vol. 14, no. 1, pp. 162–172, 1995.
[24] R. Kutka and S. Stier, "Extraction of line properties based on direction fields," *IEEE Trans. Med. Imag.*, vol. 15, no. 1, pp. 51–58, 1996.
[25] D. P. Kottke and Y. Sun, "Segmentation of coronary arteriograms by iterative ternary classification," *IEEE Trans. Biomed. Eng.*, vol. 37, no. 8, pp. 778–785, 1990.
[26] P. M. J. Zwet and P. M. J. Reiber, "A new algorithm to detect coronary boundaries: the gradient field transform," *Comput. Cardiol.*, pp. 107–110, 1992.
[27] Y. Sun, "Automated identification of vessel contours in coronary arteriograms by an adaptive tracking algorithm," *IEEE Trans. Med. Imag.*, vol. 8, pp. 78–88, March 1989.
[28] H. Shen, B. Roysam, C. V. Stewart, J. N. Turner, and H. L. Tanenbaum, "Optimal scheduling of tracing computations for real-time vascular landmark extraction from retinal fundus images," *IEEE Trans. Inform. Technol. Biomed.*, vol. 5, Mar. 2001.

---

[1]As mentioned in the beginning of Section VI, the algorithms have been deployed at the Wadsworth center since April of 1999 and have been used to trace thousands of images.

[29] A. Klein, T. K. Egglin, J. S. Pollak, F. Lee, and A. A. Amini, "Identifying vascular features with orientation specific filters and B-spline snakes," *Comput. Cardiol.*, pp. 113–116, 1994.

[30] M. Hart and L. Holly, "A method of automated coronary tracking in unsubtracted angiograms," *Comput. Cardiol.*, pp. 93–96, 1993.

[31] E. Mortensen, B. Morse, W. Barrett, and J. Udupa, "Adaptive boundary detection using live-wire two-dimensional dynamic programming," *Comput. Cardiol.*, pp. 635–638, 1992.

[32] L. Van Tran, R. C. Bahn, and J. Sklansky, "Reconstructing the cross sections of coronary arteries from biplane angiograms," *IEEE Trans. Med. Imag.*, vol. 11, pp. 517–529, 1992.

[33] T. N. Pappas and J. S. Lim, "A new method for estimation of coronary artery dimensions in angiograms," *IEEE Trans. Acoust., Speech, Signal Processing*, vol. 36, pp. 1501–1513, Sept. 1988.

[34] M. S. Zhou, L. J. Rzeszotarski, L. J. Singerman, and J. M. Chokreff, "The detection and quantification of retinopathy using digital angiograms," *IEEE Trans. Med. Imag.*, vol. 13, pp. 619–626, 1994.

[35] J. H. Van Cuyck, J. J. Gerbrands, and J. H. C. Reiber, "Automated centerline tracing in coronary angiograms," *Pattern Recog. Artifical Intell.*, pp. 169–183, 1998.

[36] S. Lu and S. Eiho, "Automated detection of the coronary arterial contours with sub-branches from an X-ray angiogram," *Comput. Cardiol.*, pp. 575–578, 1993.

[37] K. Kitamura, J. M. Tobis, and J. Sklansky, "Estimating the X-ray intercepted areas and boundaries of coronary arteries," in *Proc. Int. Conf. Pattern Recog.*, Paris, France, 1986, pp. 478–480.

[38] J. Canny, "A computational approach to edge detection," *IEEE Trans. Pattern Anal. Machine Intell.*, vol. PAMI-8, pp. 679–698, Nov. 1986.

[39] K. Bowyer, C. Kranenburg, and S. Dougherty, "Edge detector evaluation using empirical ROC curves," in *Proc. IEEE Computer Society Conference on Computer Vision and Pattern Recognition*, vol. 1, 1999, pp. 354–359.

[40] M. C. Shin, D. B. Goldgof, and K. W. Bowyer, "Comparison of edge detection algorithms using a structure from motion task," *IEEE Trans. Syst., Man, Cybern.—Part B: Cybern.*, vol. 31, pp. 589–601, Aug. 2001.

[41] G. Banker and K. Goslin, *Culturing Nerve Cells*. Cambridge, MA: The MIT Press, 1991.

[42] M. Sonka, V. Hlavac, and R. Boyle, *Image Processing, Analysis, and Machine Vision*, 2nd ed: PWS, 1998, pp. 568–580.

[43] S. H. Koslow and M. F. Huerta, Eds., *Neuroinformatics: An Overview of the Human Brain Project*. Mahwah, NJ: Lawrence Erlbaum, 1997.

[44] S. L. Senft and T. A. Woolsey, "Computer-aided analyzes of thalamo-cortical afferent ingrowth," *Cereb. Cortex*, vol. 1, no. 4, pp. 336–347, 1991.

[45] S. J. Lim, *Two-Dimensional Signal and Image Processing*. Englewood Cliffs, NJ: Prentice Hall Signal Processing Series, 1990.

[46] P. J. Rousseeuw and A. M. Leroy, *Robust Regression and Outlier Detection*. New York: Wiley, 1987.

[47] R. Hartley and A. Zisserman, *Multiple View Geometry in Computer Vision*. Cambridge, U.K.: Cambridge University Press, 2000.

[48] A. Perez, N. Dowell, L. Kam, S. Turner, H. G. Craighead, M. Isaacson, J. N. Turner, and W. Shain, "Attachment of astroglial cells to photolithographically patterned and chemically etched pillar arrays of different geometries," *J. Biomed. Mater. Res.*, vol. 51, pp. 430–441, 2000.

Ali Can (M'97) received the B.S. degree in electrical engineering from the University of Gaziantep, Turkey, in 1993, the M.S. degree in computer and systems engineering, as well as a doctorate in computer and systems engineering from Rensselaer Polytechnic Institute, Troy, NY, in 1997, and 2000, respectively.

He is currently a Postdoctoral Investigator at Woods Hole Oceanographic Institution, Woods Hole, MA. His research interests include image analysis, computer vision, robust statistics, time series analysis, image guided laser surgery and radiation therapy, medical and underwater imaging.

Dr. Can is a Member of the Microscopy Society of America. He is a recipient of the Microscopy Society of America Presidential Student Award and the Allen B. DuMont Prize for his doctoral work, both in year 2000, and the Best Paper Award at the IEEE Conference on Computer Vision and Pattern Recognition in 1999.

Sharie Lasek received the B.S. degree in molecular biology and pre-professional biology from the Florida Institute of Technology, Melbourne, FL, in 1997.

Since 1997, she has been with the Wadsworth Center for Laboratories and Research, New York State Department of Health, Albany, NY, where she is currently a Senior Technician. She handles daily operations of the Three-Dimensional Light Microscopy facility at the Wadsworth Center and is also involved with the neuro-prosthesis research project with Dr. J. Turner and Dr. W. Shain.

Donald H. Szarowski received the B.S. degree in biology from SUNY College at Fredonia in 1969.

He has been a Research Assistant at the Worcester Foundation for Experimental Biology, Shrewsbury, MA, New York Medical College, New York, NY, and Albany Medical College, Albany, NY. He is currently a Research Scientist at the Wadsworth Center for Laboratories and Research, New York State Department of Health, Albany, NY, where he is the supervisor of the Three-Dimensional Light Microscopy Facility.

Khalid A. Al-Kofahi received the B.Sc. degree in electrical and computer engineering from Jordan University of Science & Technology, Irbid, Jordan, in 1989 and the M.Sc. degree in computer engineering from Rochester Institute of Technology (RIT), Rochester, NY, in 1993. He received the Ph.D. degree in computer and systems engineering from Rensselaer Polytechnic Institute (RPI), Troy, NY, in 2000.

Since 1995, he has been working for the R&D of Thomson Legal & Regulatory, Rochester, NY. His research interests include 2-D and 3-D image processing and analysis, computer vision, information extraction, retrieval and classification, natural language processing, and machine learning.

Dr. Al-Kofahi is the recipient of the 2001 Allen B. DuMont award for scholastic achievements from RPI.

Natalie Dowell-Mesfin received the B.S. degree from SUNY, Old Westbury, where she traveled to China on a Fogarty International Grant. She received the M.S. degree from the Department of Biomedical Sciences, School of Public Health, University at Albany, where she is continuing her graduate work toward the Ph.D. degree. Her thesis research is focused on developing methods for controlling neuron process growth, especially dendrites, and synapse formation.

Ms. Dowell-Mesfin has received awards for Excellence in Research from the School of Public Health. She is a Member of the Societies for Neuroscience and Cell Biology. She has regularly presented her work at national meetings.

William Shain received the B.A. degree in biology from Amherst College, Amherst, MA, in 1966 and the Ph.D. degree in developmental/cell biology from Temple University, Philadelphia, PA, in 1972.

He was a Postdoctoral Fellow in neurobiology in Marshall Nirenberg's Laboratory at the National Institutes of Health for three years. Currently, he is a Research Scientist at the Wadsworth Center and Associate Professor in the Department of Biomedical Sciences, School of Public Health, University at Albany, NY. His laboratory uses micro- and nanofabricated devices for the study of brain and brain cell function. He is Director of a Bioengineering Research Partnership from NIBIB to study tissue integration of neural prosthetic devices and is Project Leader in the Nanobiotechnology Center, a NSF-sponsored Science and Technology Center lead by Cornell University. This project is designed to study how microfabricated-physical and patterned-chemical cues can be used to control cell attachment and growth, especially neuron axon and dendrite growth, synapse formation, and function of small networks of neurons.
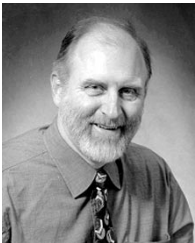
Dr. Shain is a Member of the Societies for Neuroscience, Neurochemistry, Cell Biology, and Biomaterials. He frequently serves on NIH advisory panels.

James N. Turner received the B.S. degree in engineering science in 1968 and the Ph.D. degree in biophysics in 1973 from the State University of New York at Buffalo.

He completed National Institutes of Health and National Science Foundation Postdoctoral Fellowships at the Roswell Park Memorial Institute in Buffalo, NY. Currently, he is Director of the Three-Dimensional Light Microscopy Facility and the Nanobiotechnology Program at the Wadsworth Center of the New York State Department of Health, Albany, NY, and a Platform Leader and Executive Committee Member of the Nanobiotechnology Center, a NSF sponsored Science and Technology Center lead by Cornell University, Ithaca, NY. He is Professor of Biomedical Engineering at Rensselaer Polytechnic Institute and of Biomedical Sciences in the School of Public Health of the University at Albany. He is interested in applications of light imaging methods and quantitative image analysis in biology and medicine with special emphasis on the nervous system. He is on the editorial board of Microscopy and Microanalysis, and has chaired numerous symposia in the area of 3-D microscopy both light and electron at national meetings.

Dr. Turner is a Member of the Microscopy Society of America, International Society for Analytical Cytology, and the Society for Neuroscience. He frequently serves on NIH advisory panels.

Badrinath Roysam (M'89) received the B.Tech degree in electronics engineering from the Indian Institute of Technology, Madras, India, in 1984 and the M.S. and D.Sc. degrees from Washington University, St. Louis, MO, in 1987 and 1989, respectively.

He has been at Rensselaer Polytechnic Institute, Troy, NY, since 1989, where he is currently a Professor in the Electrical, Computer and Systems Engineering Department. He is an Associate Director of the Center for Subsurface Sensing and Imaging Systems (CenSSIS)—a multiuniversity NSF-sponsored engineering research center. He also holds an appointment in the Biomedical Engineering Department. His ongoing projects are in the areas of 2-D, 3-D, and 4-D biomedical image analysis, biotechnology automation, optical instrumentation, high-speed and real-time computing architectures, and parallel algorithms.

Dr. Roysam is a Member of the Microscopy Society of America, Society for Neuroscience, and the Association for Research in Vision and Ophthalmology. He is an Associate Editor for the IEEE TRANSACTIONS ON INFORMATION TECHNOLOGY FOR BIOMEDICINE.